JOURNAL OF AIRCRAFT
Vol. 32, No. 1, January–February 1995

Neural Network Prediction of Three-Dimensional Unsteady Separated Flowfields

Scott J. Schreck*
Frank J. Seiler Research Laboratory, U.S. Air Force Academy, Colorado 80840
and
William E. Faller† and Marvin W. Luttges‡
University of Colorado, Boulder, Colorado 80903

Unsteady surface pressures were measured on a wing pitching beyond static stall. Surface pressure measurements confirmed that the pitching wing generated a rapidly evolving, three-dimensional unsteady surface pressure field. Using these data, both linear and nonlinear neural networks were developed. A novel quasilinear activation function enabled extraction of a linear equation system from the weight matrices of the linear network. This equation set was used to predict unsteady surface pressures and unsteady aerodynamic loads. Neural network predictions were compared directly to measured surface pressures and aerodynamic loads. The neural network accurately predicted both temporal and spatial variations for the unsteady separated flowfield as well as for the aerodynamic loads. Consistent results were obtained using either the linear or nonlinear neural network. In addition, fluid mechanics modeled by the linear equation set were consistent with established vorticity dynamics principles.

Nomenclature

$[A]$ = equation system square matrix, 15 × 15
a = input level for activation function saturation
$b/2$ = wing semispan length, cm
c = wing chord length, cm
c_p = pressure coefficient
$d\alpha/dt$ = pitch rate, rad/s
K = reduced frequency, $\omega c/2U_\infty$
$[k]$ = equation system constant vector, 15 × 1
t = time, s
t_{nd} = nondimensional time, tU_∞/c
U_∞ = freestream velocity, m/s
u = input to activation function
v = output from activation function
W_{ij} = neural network connection weights
x = chordwise distance from wing leading edge, cm
y = spanwise distance from splitter plate, cm
α^+ = nondimensional pitch rate, $c(d\alpha/dt)/U_\infty$

Introduction

RESEARCH in the area of unsteady flows continues to be strongly motivated by potential enhancements to aircraft performance. Subjecting wings to rapid pitching motions elicits unsteady boundary-layer separation, giving rise to the emergence and fleeting presence of energetic, large-scale vortices. While briefly present over the wing, these vortices substantially amplify the normal force generated by the wing. However, vortex shedding soon follows, causing normal force to plummet catastrophically.

The highly transient nature of unsteady separated flows renders them highly complex. Temporal complexity is exacerbated by the three dimensionality inherent to practical geometries. Spanwise nonuniformities in vortex structure and kinematics prompt corresponding spanwise variations in surface pressure distribution and normal force coefficient.[1–4]

Temporal and spatial complexity of unsteady separated flows renders them difficult to thoroughly characterize and understand. Thus far, unsteady separated flows have defied analytical solution. Although accurate, computational codes require large amounts of processor time. Experiments are also necessarily complex and time consuming. As such, the broad parameter space encompassed by three-dimensional unsteady separated flows defies exhaustive characterization by computational or experimental means. This precludes prediction and control across the broad range of conditions likely to be encountered in the flight regime.

These barriers to successful exploitation of unsteady separated flows can be attacked using neural networks. Neural networks possess the capability to model temporal and spatial dependencies of complex, nonlinear systems across broadly varying conditions given only limited information. Previous research has shown that neural networks are effective in developing models of complex, nonlinear systems.[5–8] Other work has demonstrated the utility of neural networks for general control system design.[9–11] Current research has shown that neural networks can predict flowfield evolution under static[12–14] and dynamic[15–17] conditions. Recently, neural networks have also been used to construct accurate models and effect real-time control of time-dependent, unsteady separated flowfield evolution.[18]

The current effort examines neural network modeling of the spatial and temporal dependencies associated with three-dimensional unsteady separated flows. Results show that the neural network is capable of accurately predicting unsteady surface pressure fields, as well as aerodynamic coefficients in real-time fashion and across broadly varying conditions. In addition, the neural network is also shown to be a powerful tool for identification of the fluid mechanics responsible for three-dimensional unsteady separated flows.

Experimental Methods

Unsteady Surface Pressure Measurement

Unsteady surface pressure measurements were performed in the Frank J. Seiler 0.91- × 0.91-m low-speed wind tunnel

Presented as Paper 93-3426 at the AIAA 11th Applied Aerodynamics Conference, Monterey, CA, Aug. 9–11, 1993; received Dec. 2, 1993; revision received May 4, 1994; accepted for publication May 4, 1993.

*Unsteady Aerodynamics Task Manager, 2354 Vandenberg Drive, Suite 6H79. Member AIAA.
†University Research Fellow, Department of Aerospace Engineering Sciences. Member AIAA.
‡Professor of Aerospace Engineering Sciences, Department of Aerospace Engineering Sciences. Member AIAA.

located at the U.S. Air Force Academy. A rectangular planform wing with 15.24 cm chord length was fabricated from hollow aluminum NACA 0015 airfoil stock. The basic wing was equipped with a fitting on the outboard end that permitted arbitrary length extensions to be added. Fifteen miniature pressure transducers were installed inside the hollow basic wing model. These transducers were close-coupled to the wing surface through pressure ports located along the chord line, 3.05 cm inboard of the basic wing end. Pressure transducer signals were low pass filtered (300-Hz cutoff) and amplified by a gain of 500. The resulting signals were sampled and digitized by the data acquisition system.

A circular aluminum splitter plate, 30.48 cm in diam and 0.64 cm thick, was machined to a sharp edge around the plate perimeter. The splitter plate had a NACA 0015 cutout centered in it, which allowed it to slide onto the wing and be positioned at arbitrary span locations. To effectively move the pressure ports along the wingspan, the splitter plate was first positioned at the desired distance from the pressure ports. Then, a tip extension of the correct length was added to the basic wing, bringing the span length to 30.48 cm and maintaining aspect ratio constant at 2.0. The chordwise row of pressure ports was successively moved to nine span locations, effectively distributing pressure ports over the wing surface as shown in the Fig. 1 planform view of the model. All tip extensions used in this experiment terminated in a square tip.

In Fig. 1, spanwise pressure port locations range from 0.0 to 0.80 span outboard of the splitter plate. Chordwise pressure port locations range from 0.0 to 0.90 chord, with 0.0 chord corresponding to the wing leading edge. Unsteady surface pressures measured at these port locations were contour plotted using a linear interpolation between adjacent grid points in both the chordwise and spanwise directions.

For constant rate pitching, the model was driven by a 3.5-hp stepper motor through a 4:1 reduction gear linkage. Sinusoidal pitching was driven by a scotch yoke powered by a $\frac{3}{4}$-hp shunt wound dc motor. In both cases, the wing-splitter plate configuration was connected to the drive system and supported in the test section by a steel shaft 2.86 cm in diam. The independent variables explored in the surface pressure experiments included nondimensional pitch rates 0.01, 0.02, 0.05, 0.075, 0.10, 0.15, and 0.20 (constant rate pitching), as well as reduced frequency 0.25 (sinusoidal pitching). Data were acquired at nine spanwise pressure port locations 0.0, 0.05, 0.10, 0.15, 0.25, 0.375, 0.50, 0.625, and 0.80 span outboard of the splitter plate. Wing pitch axis was located at 0.25 chord throughout the experiment. Test section velocity was held constant at 9.14 m/s, yielding a chord Reynolds number of 6.9×10^4.

Constant rate pitching encompassed 63 combinations of nondimensional pitch rate and spanwise pressure port location. For sinusoidal pitching, four combinations were investigated. For each combination, surface pressures were sampled during 20 consecutive wing pitch motions and ensemble-averaged to obtain ensemble-averaged data sets. Surface pressures were also sampled for single pitch motions to obtain single pitch realizations of the surface pressure data.

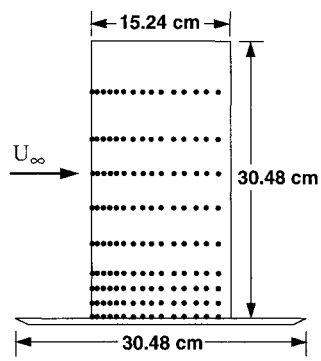

Fig. 1 Effective pressure port distribution over the model surface.

Neural Network Development

The digitized, unsteady surface pressure records were subsequently used to define a neural network model[16,17] of the three-dimensional, unsteady separated flowfield generated by the pitching wing-splitter plate configuration. The neural network consisted of an empirically determined[19] feed-forward architecture having an input layer, two hidden layers, and an output layer. Both the input and output layers contained 15 activation units, one for each pressure port location at a single spanwise location. Each hidden layer consisted of 32 activation units and included bias units. The neural network architecture is shown schematically in Fig. 2.

A time independent pattern association paradigm was adopted that related network inputs to outputs. Each network input was a 15-element vector that represented the ensemble averaged unsteady surface pressure distribution at some arbitrary time t in the pitch motion. Targeted output vectors also consisted of 15 elements each, and represented predictions of unsteady surface pressure distribution one sample after the input vector, at time $(t + \Delta t)$.

In this paradigm, Δt was chosen relative to the time scales that govern unsteady separated flowfield evolution.[1] The Δt used in the current work is abbreviated relative to these physical time scales. However, this Δt is extended compared to time step lengths required in recent finite difference computations for the same flowfield.[20] To date for this problem, no solutions have been shown that employ classical linear regression techniques.

To predict surface pressure distributions at $(t + \Delta t)$, only surface pressure data at t were used as network inputs. A highly accurate recurrent, time-dependent neural network has been developed that reveals no dependence on $(t - \Delta t)$, $(t - 2\Delta t)$, . . . , $(t - n\Delta t)$.[18] Given this result, no accuracy improvement could be expected for predictions at $(t + \Delta t)$ using surface pressure information prior to t.

To correctly predict unsteady surface pressure distributions, the neural network required training. Training was based upon a supervised gradient descent, or backpropagation, algorithm.[21] Data used to train the neural network comprised a limited subset of the full experimental data range. The training set included only ensemble-averaged data for five of the seven nondimensional pitch rates, and only one of the nine span locations. Data collected at nondimensional pitch rates 0.01, 0.02, 0.05, 0.10, and 0.20, at 0.375 span outboard of the splitter plate were used for network training. Neither data acquired during single pitch motions nor sinusoidal pitching data were used during network training.

During training, the five data sets were presented randomly with the stipulation that each data set be presented an equal number of times. Initial connections weights between units were set randomly between -0.25 and 0.25. Following each presentation, these weights were adjusted based upon the backpropagation algorithm. Training continued until the error between the predicted surface pressure distribution and the experimental data was less than 5% for all five training sets.

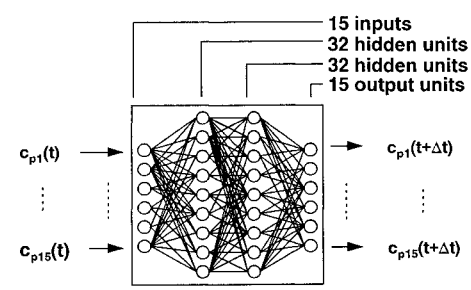

Fig. 2 Schematic of neural network architecture.

Training required approximately 10 h on a DEC VAX 3600. Thus, following training, the neural network model should accurately predict the unsteady surface pressure distribution at time $(t + \Delta t)$ given only the pressure distribution at arbitrary t.

For the nonlinear neural network, a standard sigmoidal activation function, $v = 1/(1 + e^{-u})$, was used. For the linear network, a novel quasilinear function defined in Eq. (1) was adopted. As implied by Eq. (1), activation units were not permitted to maintain a saturated $v = 0.0$ or $v = 1.0$ output during training. If an activation unit did saturate during training, then prior to the next training presentation, the weights (W_{ij}) were halved $[0.5(W_{ij})]$ on all connections entering the saturated unit. Thus, at training completion, all activation units functioned within the linear range of the activation function:

$$v = 0.0, \quad W_{ij} = 0.5(W_{ij}) \quad \text{for} \quad u < -a \quad (a = 4.0) \tag{1a}$$

$$v = 0.5(u/a) + 0.5 \quad \text{for} \quad -a \le u \le a \quad (a = 4.0) \tag{1b}$$

$$v = 1.0, \quad W_{ij} = 0.5(W_{ij}) \quad \text{for} \quad u > a \quad (a = 4.0) \tag{1c}$$

The activation function described by Eq. (1) is not the typical linear sigmoidal activation function. As shown herein, this particular form of linear activation function enables extraction of a linear equation system from the neural network architecture. As such, the architecture used in the current work should not be confused with three or four layer networks employing the more common linear sigmoidal activation function.

The output of each activation unit was constrained to lie within the linear region of the activation function. Thus, the contribution of each input unit to each output unit remained linearly separable from all other inputs. Therefore, the contribution of each individual input unit to each individual output unit was uniquely determined. With training complete and all connection weights determined, it was possible to use the network weight matrices to determine a single coefficient describing the contribution of each input unit to each output unit. For 15 inputs and 15 outputs, 225 such coefficients were organized into a 15 × 15 matrix $[A]$, and a 15-element constant vector $[k]$. This linear equation system, shown in Eq. (2), acts upon the input vector representing the measured surface pressure distribution at t. The output vector is then the surface pressure distribution predicted by the neural net at $(t + \Delta t)$:

$$[A][c_p(t)] + [k] = [c_p(t + \Delta t)] \tag{2}$$

The linear neural network and the linear equation system yielded identical solutions during all further analyses. Thus, the equation system was used in lieu of the neural network.

Results

Unsteady Surface Pressure Measurements

Pitch angle histories are shown in Fig. 3. All seven constant rate histories begin at a pitch angle of 0.0 deg and end at 60.0 deg. Sinusoidal pitching begins at the maximum pitch angle of 20.0 deg and declines to the minimum angle of 0.0 deg one-half cycle later. The beginning of these histories coincides with the inception of surface pressure data acquisition. Thus, the plots in Fig. 3 can be used in conjunction with subsequent plots to convert nondimensional time to instantaneous wing pitch angle.

Figure 4 shows representative surface pressure coefficient topologies for nondimensional pitch rate 0.10. The three-frame series documents unsteady flowfield development on the wing upper surface at nondimensional times 5.28, 6.30, and 7.26. Lower surface pressure fields were characterized by mild two-dimensional pressure gradients that underwent limited temporal evolution, and will not be presented here. Each of the three frames in Fig. 5 is identical in format, with the free-stream flowing from bottom to top. Chord location 0.0 corresponds to the wing leading edge, and the splitter plate corresponds to span location 0.0.

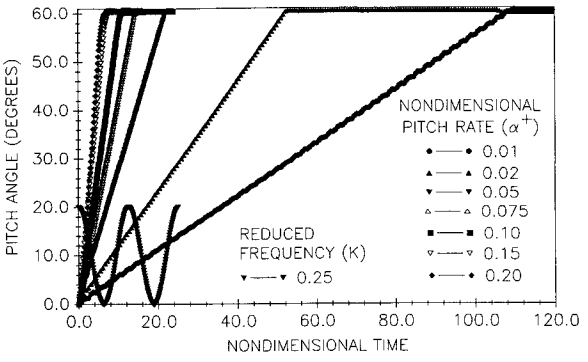

Fig. 3 Wing pitch angle histories for the experimental parameter range.

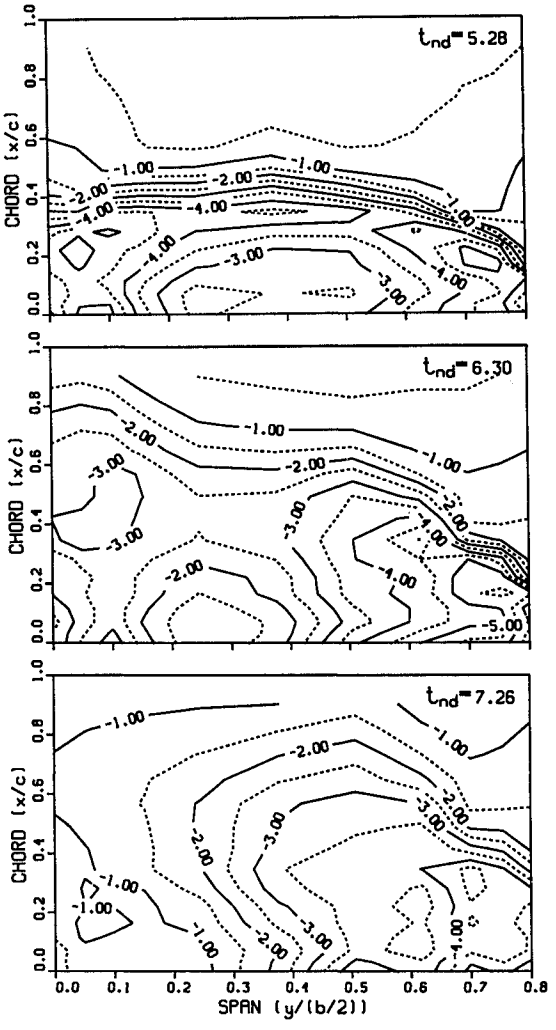

Fig. 4 Surface pressure topologies for $\alpha^+ = 0.10$, at $t_{nd} = 5.28$, 6.30, and 7.26.

Frame 1 (top panel) of Fig. 4 depicts surface pressure topology at nondimensional time 5.28, 1.32 nondimensional time units after leading-edge vortex initiation. This topology is dominated by an arc-shaped suction ridge that begins near the intersection of the splitter plate and wing leading edge. The suction ridge proceeds outboard across the wingspan, curves back to 0.33 chord at center span, and again ap-

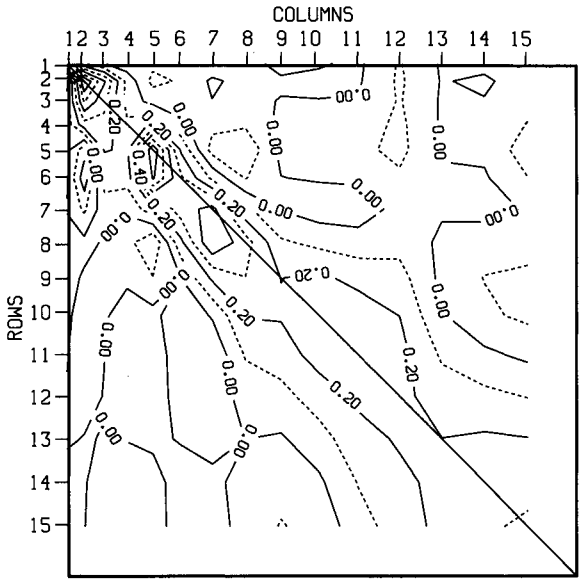

Fig. 5 Contour plot of [A] matrix elements. Grid spacing in both the horizontal and vertical directions is consistent with chordwise pressure port spacing on the wing.

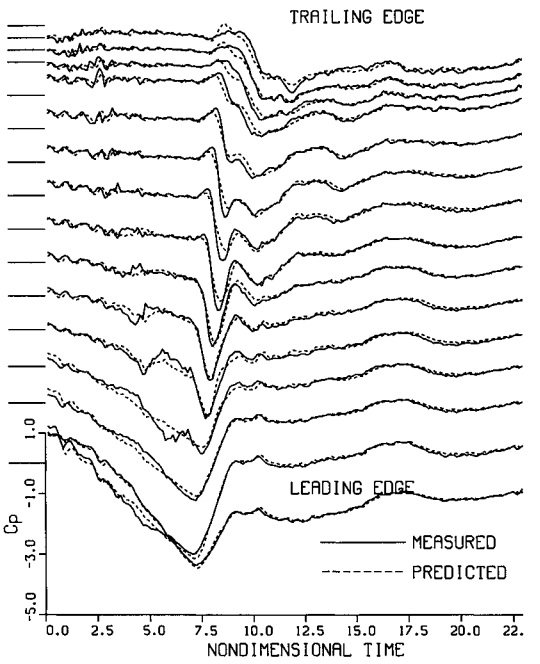

Fig. 6 Measured and predicted ensemble averages of surface pressure history for $\alpha^+ = 0.05$ at $y/(b/2) = 0.375$.

proaches the leading-edge 0.80 span outboard of the splitter plate. Suction ridge magnitude is generally uniform along the length of the ridge.

The frame 2 topology (middle panel) corresponds to nondimensional time 6.30, and shows the suction ridge remains arc-shaped only outboard of 0.50 span. Inboard of 0.50 span, the suction ridge proceeds inboard and slightly aft over the planform. The outboard end of the ridge still appears to terminate near the wing leading edge. Near the ridge center, magnitude has been suppressed, but remains relatively high both inboard and outboard of center.

Frame 3 (bottom panel) in Fig. 4 shows surface pressure topology at nondimensional time 7.26. The topology consists principally of a straight, broad suction ridge extending from the leading edge near the wingtip to the trailing edge near the splitter plate. Ridge magnitude is greatest near the wingtip and decreases monotonically to a minimum near the splitter plate.

Network Architecture and Equation System Definition

Neural network training was completed and the weight matrices were subsequently compressed into the $[A]$ and $[k]$ matrices of Eq. (2). A contour plot was applied to the elements contained in the Eq. (2) $[A]$ matrix. Contour plot grid point spacing in both the horizontal and vertical directions was consistent with chordwise pressure port locations on the airfoil. This contour plot is shown in Fig. 5. The line drawn between the upper left and lower right corners of the contour plot represents the matrix diagonal.

Figure 5 reveals a prominent ridge extending from the upper left to lower right corner of the plot. This signifies that $[A]$ matrix element values are significantly greater near the matrix diagonal. On and slightly below the matrix diagonal, three distinct local maxima are indicated by three sets of concentric contours. The first is centered at element (row, column) = (1, 1), the second is located at element (row, column) = (5, 5), and the third occurs at element (row, column) = (8, 7). A fourth set of concentric contours is evident off the diagonal, at element (row, column) = (6, 2), and represents a local minimum. Contour spacing is most dense near the upper left corner of the plot, indicating steeper gradients in matrix element values. Contours are spaced more sparsely as distance from the upper left corner increases, consistent with more gradual gradients.

Unsteady Flowfield Predictions

Network prediction performance was tested for both the nonlinear neural network and the linear equation system. For each of the 63 combinations of nondimensional pitch rate and span location, testing encompassed single pitch realizations as well as ensemble-averaged data records. Network predictive accuracy was also tested for sinusoidal wing pitching. For all cases, predicted and measured data were compared directly. Thus, following training, it was possible to determine not only how well the models predicted the data used for training, but how well the models generalized to surface pressure data for nondimensional pitch rates, span locations, single pitch realizations, and pitch motions not used for training.

Figures 6–10 show representative comparisons between measured unsteady surface pressure data and predictions generated using the linear equation system. Each plot contains solid traces, representing measured surface pressure data, and dashed traces, corresponding to neural network predicted surface pressures. In all plots, the bottom traces, corresponding to pressure port 1, record the surface pressure history at the wing leading edge. Traces located farther up on the graph correspond to pressure port locations 2–15, farther aft on the wing suction surface. The abscissa is nondimensional time and the ordinate is pressure coefficient. At the left border of the plot, 15 horizontal hash marks denote 0.0 pressure coefficient for the 15 pairs of traces.

Wing pitching elicited dramatic temporal and spatial pressure fluctuations over the wing surface. In Figs. 6–10, four phases of surface pressure evolution are common to all data records in this investigation. First, wing pitching begins at nondimensional time 0.0 and is accompanied by constant rate pressure reduction at pressure ports located on the forward portion of the wing. Surface pressures decrease more quickly at port locations farther forward on the wing. Also during this phase, surface pressure decrease is interrupted by subdued pressure fluctuations that occur later for port locations farther forward on the wing. Second, the rate of surface pressure decrease is significantly accelerated at midchord port locations, while surface pressures continue to decrease at the initial rate at port locations on the forward portion of the wing. Third, surface pressure reductions culminate in briefly persisting minima, or suction spikes, that attain pressure coefficient values between approximately -4.0 and -7.0 for the

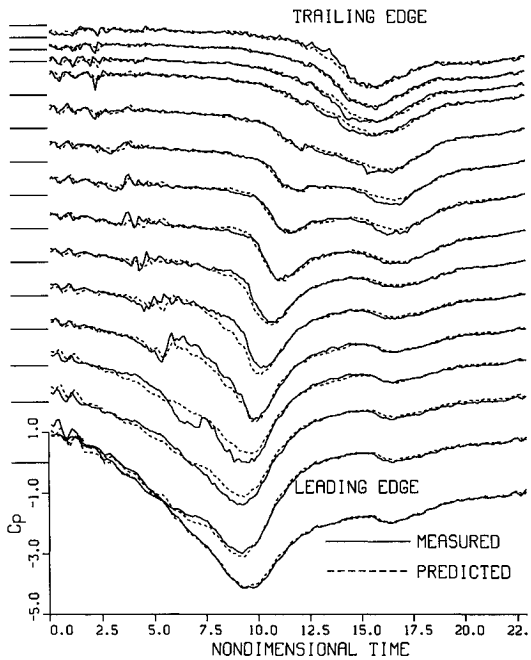

Fig. 7 Measured and predicted ensemble averages of surface pressure history for $\alpha^+ = 0.05$ $y/(b/2) = 0.80$.

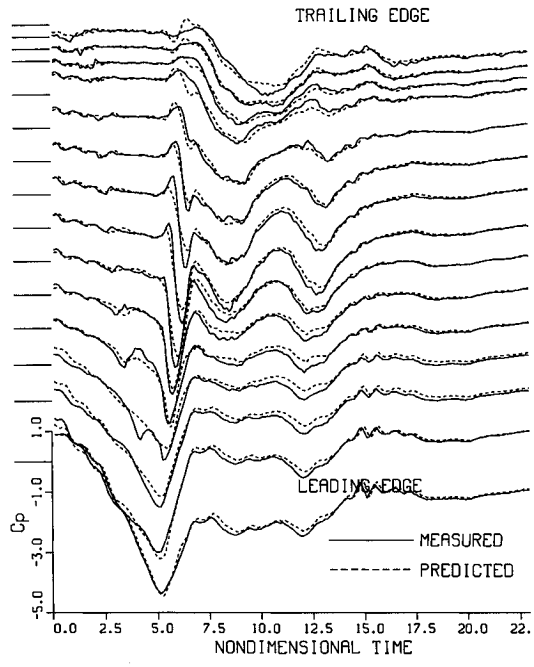

Fig. 8 Measured and predicted ensemble averages of surface pressure history for $\alpha^+ = 0.075$ at $y/(b/2) = 0.80$ span outboard of the splitter plate.

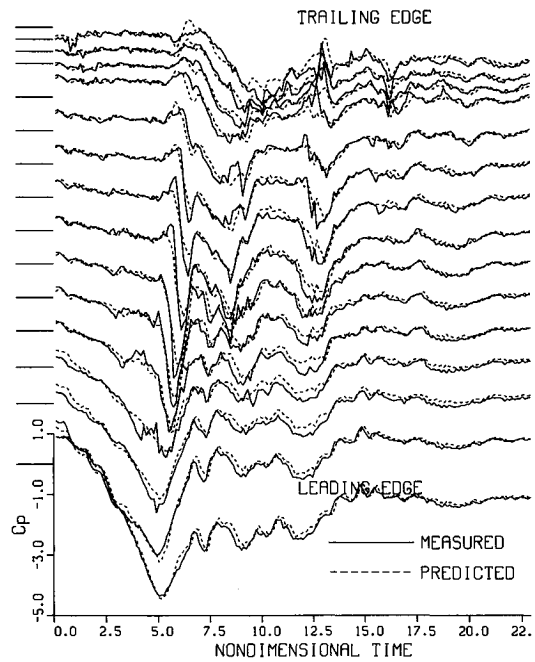

Fig. 9 Measured and predicted single pitch realizations of surface pressure history for $\alpha^+ = 0.075$ at $y/(b/2) = 0.375$ span outboard of the splitter plate.

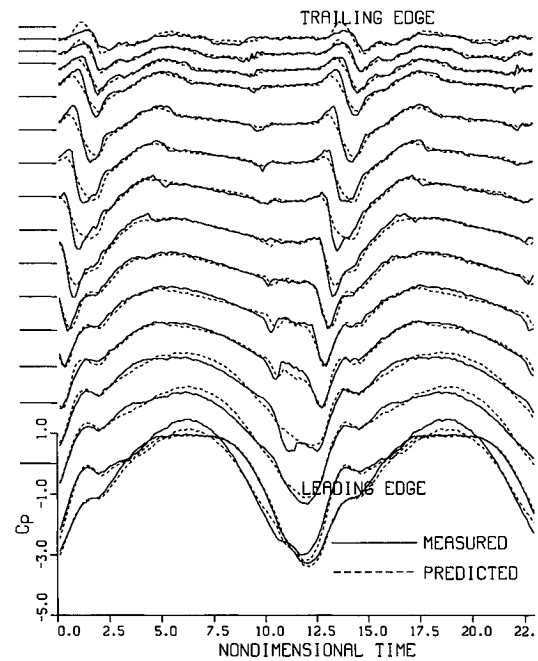

Fig. 10 Measured and predicted ensemble averages of surface pressure history for $K = 0.25$ at $y/(b/2) = 0.375$.

parameter range investigated. These pressure minima occur progressively later in the pitch motion at pressure port locations farther aft on the wing. Finally, after attaining minimum values, surface pressures increase again to levels approximating those earlier in the pitch motion.

Figure 6 contains ensemble-averaged data for nondimensional pitch rate 0.05 at 0.375 span outboard of the splitter plate. This nondimensional pitch rate and span location were included in the training set, since this is one of the five data sets used to train the network. Measured and predicted surface pressures show close agreement throughout the entire data record. However, during initial pressure decrease, between nondimensional times 3.0 and 6.0, the network has difficulty predicting the pressure fluctuations superimposed on the constant rate decrease at port locations 4–7. Pressure minima magnitudes and times of occurrence are accurately predicted for the first seven port locations. In contrast, at port locations 8, 9, and 10, minimum pressure coefficient magnitudes are underpredicted by approximately 0.2, while pressure minimum occurrence times lag measured times by 0.25 nondimensional time units.

Figure 7 shows ensemble-averaged data for nondimensional pitch rate 0.05 at a span location 0.80 span outboard of the splitter plate. The training set included nondimensional pitch rate 0.05, but did not include span location 0.80. Once again, surface pressures are accurately predicted over most of the data record. Between nondimensional times 6.0 and 10.0, pressure reduction is underpredicted at ports 3 and 4, but

overpredicted at ports 5 and 6. The network accurately predicts pressure minimum occurrence times for all ports. However, minimum pressure magnitudes are underpredicted by 0.3 at ports 3 and 4, and overpredicted by 0.2 at port 6.

Figure 8 contains ensemble-averaged data for nondimensional pitch rate 0.075 at 0.80 span outboard of the splitter plate. Neither span location 0.80 nor nondimensional pitch rate 0.075 was included in the training set. Predictions are, again, of high accuracy over the majority of the data record. Minor errors occur at port locations 3–6, between nondimensional times 3.0 and 5.0, as the network attempts to predict the fluctuations superimposed on the initial pressure reduction. Subsequently, pressure coefficient minimum magnitude is overpredicted by 0.2 at port 2, and underpredicted by approximately 0.4 at ports 3 and 4, as well as at ports 6–9. Predicted pressure minimum occurrence times lag measured times at ports 1–5 and at ports 7, 9 and 10, but by only 0.15 nondimensional time units.

Figure 9 displays single pitch motion data for nondimensional pitch rate 0.075 at a span location 0.375 span outboard of the splitter plate. All previous data sets consisted of ensemble averages computed from data acquired over 20 consecutive pitch motions. Single pitch motion data were not used to train the neural network, yet predictions remain highly accurate over the majority of the data record. Minor prediction errors are apparent at port locations 2–6, between nondimensional times 3.0 and 5.0, during variations associated with initial pressure reduction. During this time, pressure minima magnitudes are underpredicted by approximately 0.2 at ports 3, 6, 7, and 8, and overpredicted by 0.15 at ports 2 and 5. Predicted pressure minimum occurrence times lag measured times at ports 2, 7, 9, and 10, by 0.15 nondimensional time units. Even low amplitude, high-frequency pressure variations not evident in the ensemble-averaged training data are predicted with moderate accuracy by the network.

Figure 10 contains ensemble-averaged data for two cycles of sinusoidal pitching at reduced frequency 0.25, collected at 0.375 span. At nondimensional time 0.0, the wing is pitched up at the maximum angle of 20.0 deg. One-half cycle later, at nondimensional time 6.28, the wing has reached the maximum pitch down angle of 0.0 deg. Pressure data acquired during sinusoidal pitching were not used in network training. In spite of this, network predictive accuracy remains high throughout the data record. Pressure minima magnitudes are underpredicted by 0.2–0.4 at ports 3, 4, 8, 9, 11, and 12. Detectable lags in predicted pressure minimum occurrence times are confined to ports 8–12, and are about 0.2 nondimensional time units. The longest prediction lag is 0.5 nondimensional time units at port 9.

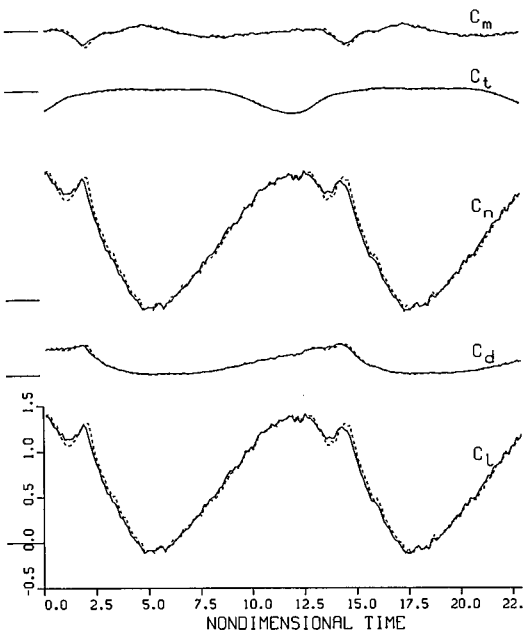

Fig. 11 Unsteady aerodynamic loads obtained by integrating measured and predicted ensemble averages of surface pressure histories for $K = 0.25$ at $y/(b/2) = 0.375$.

The unsteady surface pressures shown in Fig. 10 were integrated to compute aerodynamic force and moment coefficients. The resulting unsteady aerodynamic load data for sinusoidal pitching, at reduced frequency 0.25 and 0.375 span, are presented in Fig. 11. Figure 11 contains solid traces, representing coefficients computed from measured surface pressure data, and dashed traces, corresponding to coefficients computed from neural network predictions. The bottom pair of traces corresponds to lift coefficient, whereas traces farther up represent coefficients of drag, normal force, tangential force, and quarter-chord pitching moment. The abscissa is nondimensional time, and the ordinate is pressure coefficient. At the left border of the plot, 5 horizontal hash marks denote 0.0 aerodynamic coefficient for the 5 pairs of traces.

Figure 11 demonstrates that integrating unsteady surface pressure predictions, shown in Fig. 10, yields extremely accurate unsteady aerodynamic force and moment predictions. Only small errors in coefficient magnitude are observed. Prediction lags are similarly subdued, being no greater than 0.1 nondimensional time units.

Discussion

Unsteady Surface Pressure Measurements

Pitching the wing-splitter plate configuration beyond static stall generated an unsteady separated flowfield that has been characterized in detail in previous experiments.[1-4] For all nondimensional pitch rates and reduced frequencies included in the current investigation, the unsteady surface pressure field evolves rapidly in time, and varies radically in response to changes in either dynamic pitch parameter or span location. Figure 4 illustrated the severity of spanwise variation, or three dimensionality, in the surface pressure field on the pitching wing-splitter plate configuration. Clearly, radical differences distinguish surface pressure distributions at 0.375 span, the training data source, from those at the other eight span locations. Similarly, prominent distinctions separate surface pressure evolution for the five nondimensional pitch rates used in training, from surface pressure evolution at the remaining two nondimensional pitch rates, for sinusoidal pitching and for single pitch realizations.

Network Architecture and Equation System Definition

As shown by Eq. (2), the $[A]$ matrix operates upon measured surface pressure distributions at t to predict surface pressure distributions at time $(t + \Delta t)$. Thus, the $[A]$ matrix models the vorticity dynamics governing unsteady flowfield evolution over the time interval Δt. $[A]$ matrix structure was consistent with vorticity dynamics principles known to govern spatial and temporal evolution of unsteady separated flowfields.

In the Fig. 5 contour plot, the diagonal ridge was a prominent feature consisting of large $[A]$ matrix elements, thus having considerable significance regarding flowfield evolution. Consistent with matrix multiplication, the ridge indicated that the surface pressure predicted for $(t + \Delta t)$ at any given pressure port location was most strongly influenced by surface pressure measured at t in the same chord vicinity. However, the ridge was displaced below the matrix diagonal. Thus, predicted surface pressure at each chord location was more strongly impacted by events occurring upstream of that location, rather than downstream. This bias is consistent with net downstream convection of accumulated vorticity imposed by the freestream.[22,23]

The maximum centered at (row, column) = (1, 1) in the $[A]$ matrix was also physically significant. Near the $[A]$ matrix

center, the ridge was displaced below the matrix diagonal, consistent with downstream leading-edge vortex convection over the midchord. However, at the upper left corner of the matrix, the ridge coincides with the matrix diagonal, indicating arrested leading-edge vortex convection. Furthermore, the largest element in the [A] matrix is located at (row, column) = (1, 1) and signifies persistence of very low surface pressure at the leading edge. This indicates that vortex convection is arrested near the wing leading edge by low surface pressures at the leading edge. Acharya and Metwally[24] have determined that sustained low pressure at the leading edge retards vortex convection.

Unsteady Flowfield Predictions

Figures 6–10 showed that the linear equation system generated by the neural net predicted unsteady surface pressures over a broad range of conditions with remarkable accuracy. The neural network was trained using only ensemble-averaged data corresponding to constant rate pitching at nondimensional pitch rates 0.01, 0.02, 0.05, 0.10, and 0.20, all at 0.375 span outboard of the splitter plate.

Clearly, the linear equation system is capable of accurately predicting data included in the network training set, as shown in Fig. 6. However, it is equally capable of generalizing to novel span locations, as demonstrated in Fig. 7. In addition, Fig. 8 established that predictions remain accurate when generalizing simultaneously to novel nondimensional pitch rates and novel span locations. Figure 9 showed that the linear equation system is also capable of accurately predicting single pitch surface pressure data, even though the network was trained using only ensemble-averaged data. Finally, Fig. 10 showed that the linear equation system successfully generalizes to novel wing pitch motions. In Fig. 10, surface pressures were accurately predicted for sinusoidal wing pitching, even though the network was trained only on constant rate pitching cases.

The unsteady surface pressures shown in Fig. 10 were integrated to compute unsteady aerodynamic coefficients. These results were presented in Fig. 11 and showed that network surface pressure predictions could be used to accurately predict coefficients of lift, drag, normal force, tangential force, and quarter-chord pitching moment. The subdued surface pressure prediction errors seen in Figs. 6–10 were further attenuated when the surface pressures were integrated to obtain the unsteady aerodynamic coefficients.

Surface pressure predictions presented in Figs. 6–10 showed minor, though detectable, degradation at port locations 2–6 as pressures declined toward minimum levels early in the pitch motion. These pressure port locations were located between 0.025 and 0.217 chord. Previous experiments[2] have shown that the leading-edge vortex initiates near these chord locations and during these times in the pitch motion. Vortex initiation is prompted by unsteady separation that is a strongly viscous and, therefore, highly nonlinear process. However, the neural network uses a linear activation function to generate a linear equation system for prediction. Thus, prediction inaccuracies should be expected at locations and during times dominated by strongly viscous processes.

The linear equation system predicted magnitudes of surface pressure minima with good accuracy in Figs. 6–10. The maximum error observed in magnitude prediction constituted less than 10% of the pressure minimum magnitude. However, errors of this magnitude were restricted in spatial and temporal extent. Prediction errors for most port locations and times were on the order of 1%. Pressure minimum occurrence times were also predicted with good accuracy. Occurrence time prediction error never exceeded 0.5 nondimensional time units and, for most port locations and times, was undetectable within the limits imposed by the temporal discretization. Prior research has established that leading-edge vortex passage is responsible for pressure minima like those observed in Figs. 6–10.[25] This indicates that the linear equation system faithfully models the dynamics of the vortex-surface interaction induced by the convecting leading-edge vortex.

Although overall prediction accuracy was shown to be excellent in Figs. 6–10, the linear equation system does not impose appreciable penalties in terms of computational time. Dimensions of the linear equation system shown in Eq. (2) are small, and the number of operations required to calculate a prediction is modest. Given current processor capabilities, unsteady pressure predictions performed using the linear system can be considered real-time.

Conclusions

A wing-splitter plate configuration was pitched beyond static stall for a range of nondimensional pitch rates. The resulting unsteady separated flowfields evolved rapidly and exhibited prominent temporal fluctuations. Unsteady surface pressure histories varied substantially in response to changes in either nondimensional pitch rate or span location.

Neural networks employing novel quasilinear activation functions were trained using ensemble-averaged unsteady surface pressure measurements. Use of quasilinear activation functions preserved separability and allowed extraction of a linear equation system from the trained network. Unsteady surface pressure predictions were identical for the linear network and the linear equation system.

The linear equation system contains an [A] matrix that models unsteady separated flowfield evolution over the time interval Δt. Crucial leading-edge vortex kinematics and vorticity dynamics are encoded in the [A] matrix. In spite of a restricted training set, this [A] matrix describes kinematics and dynamics for a broad range of nondimensional pitch rates and span locations. Predictive accuracy of the linear equation system for novel data testifies to this.

Linear equation system prediction accuracy was tested for training data, novel span locations, novel nondimensional pitch rates, single pitch motion data, and for novel sinusoidal pitch motions. Throughout the test range, prediction accuracy demonstrated by the linear equation system was excellent. Prediction errors were observed in conjunction with unsteady separation, which is dominated by viscous processes and is thus highly nonlinear. However, kinematics of the mature leading-edge vortex were predicted with excellent accuracy.

Excellent prediction accuracy of the linear equation system allowed unsteady surface pressures to be integrated, yielding unsteady aerodynamic load data of equally high accuracy.

Linear equation system dimensions are small, and the number of operations required to calculate a prediction is modest. Given current processor capabilities, unsteady surface pressure predictions performed using the linear system can thus be considered real-time.

Issues of comprehension and real-time prediction over a broad parameter space remain crucial prerequisites for control of unsteady separated flows. The current investigation has examined neural network architectures, as well as a linear equation system derived from these networks. The attributes inherent in the linear systems render them powerful tools for understanding and real-time prediction of unsteady separated flows across broad parameter ranges. Work in progress will extend the prediction interval and reduce the number of required inputs while maintaining high prediction accuracy and real-time capability. These and similar methodologies will play a major role in granting radically enhanced agility to future aircraft.

References

[1]Robinson, M., Walker, J., and Wissler, J., "Unsteady Surface Pressure Measurements on a Pitching Rectangular Wing," *Proceedings of Workshop II on Unsteady Separated Flow*, U.S. Air Force Academy, CO, 1988, pp. 225–237.

[2]Schreck, S., Addington, G., and Luttges, M., "Flow Field Structure and Development Near the Root of a Straight Wing Pitching at Constant Rate," AIAA Paper 91-1793, June 1991.

[3]Schreck, S., and Helin, H., "Unsteady Vortex Dynamics and Surface Pressure Topologies on a Pitching Wing," AIAA Paper 93-0435, Jan. 1993.

[4]Lorber, P., Covino, A., and Carta, F., "Dynamic Stall Experiments on a Swept Three-Dimensional Wing in Compressible Flow," AIAA Paper 91-1795, June 1991.

[5]Chu, S., Shoureshi, R., and Tenorio, M., "Neural Networks for System Identification," *IEEE Control Systems Magazine*, April 1990, pp. 31–34.

[6]Chen, S., Billings, S., and Grant, P., "Nonlinear System Identification Using Neural Networks," *International Journal of Control*, Vol. 51, No. 6, 1990, pp. 1191–1214.

[7]Ljung, L., "Issues in System Identification," *IEEE Control Systems Magazine*, Jan. 1991, pp. 25–29.

[8]Parlos, A., Atiya, A., and Sunkel, J., "Parameter Estimation in Space Systems Using Recurrent Neural Networks," AIAA Paper 91-2716, Aug. 1991.

[9]Nguyen, D., and Widrow, B., "Neural Networks for Self-Learning Control Systems," *IEEE Control Systems Magazine*, April 1990, pp. 18–23.

[10]Narenda, D., and Mukhopadhyay, S., "Intelligent Control Using Neural Networks, *IEEE Control Systems Magazine*, April 1992, pp. 11–18.

[11]Sartori, M., and Antsaklis, P., "Implementations of Learning Control Systems Using Neural Networks," *IEEE Control Systems Magazine*, April 1992, pp. 49–57.

[12]Ha, C. M., "Neural Networks Approach to AIAA Aircraft Control Design Challenge," AIAA Paper 91-2672, Aug. 1991.

[13]Troudet, T., Garg, S., and Merrill, W., "Neural Network Application to Aircraft Control System Design," AIAA Paper 91-2715, Aug. 1991.

[14]Linse, D., and Stengel, R., "Identification of Aerodynamic Coefficients Using Computational Neural Networks," AIAA Paper 92-0172, Jan. 1992.

[15]Rokhsaz, K., and Steck, J., "Application of Artificial Neural Networks in Nonlinear Aerodynamics and Aircraft Design," Society of Automotive Engineers Paper 932533, Sept. 1993.

[16]Faller, W., Schreck, S., and Luttges, M., "Quasi-Linear Neural Networks: Application to the Prediction and Control of Unsteady Aerodynamics," Society of Photo-Optical Instrumentation Engineers Paper 1965-40, April 1993.

[17]Faller, W., Schreck, S., and Luttges, M., "Modeling Three-Dimensional Unsteady Aerodynamics with Neural Networks," *IEEE Transactions on Neural Networks* (to be published).

[18]Faller, W., Schreck, S., and Luttges, M., "Real-Time Prediction and Control of Three-Dimensional Unsteady Separated Flow Fields Using Neural Networks," AIAA Paper 94-0532, Jan. 1994.

[19]Faller, W., Schreck, S., and Luttges, M., "Temporal Coding in Neural Networks," Society of Photo-Optical Instrumentation Engineers Paper 1966-11, April 1993.

[20]Newsome, R. W., "Numerical Simulation of Wing-Wall Juncture Flow for a Pitching Wing," AIAA Paper 93-3401, Aug. 1993.

[21]Rumelhart, D., Hinton, G., and Williams, R., "Learning Internal Representations by Error Propagation," *Parallel Distributed Processing*, 1st ed., Vol. 1, MIT Press, Cambridge, MA, 1986, pp. 322–328.

[22]Luttges, M., and Kennedy, D., "Initiation and Use of Three-Dimensional Unsteady Separated Flows," Workshop II on Unsteady Separated Flow, U.S. Air Force Academy, CO, 1988, pp. 211–222.

[23]Reynolds, W., and Carr, L., "Review of Unsteady, Separated and Driven Flows," AIAA Paper 85-0527, March 1985.

[24]Acharya, M., and Metwally, M., "Evolution of the Unsteady Pressure Field and Vorticity Production at the Surface of a Pitching Airfoil," AIAA Paper 90-1472, June 1990.

[25]Walker, J., Helin, H., and Chou, D., "Unsteady Surface Pressure Measurements on a Pitching Airfoil," AIAA Paper 85-0532, March 1985.